PAPER

Efficient capture of strontium from aqueous solutions using graphene oxide–hydroxyapatite nanocomposites†

Tao Wen,[a,b] Xilin Wu,[b] Mancheng Liu,[b] Zhouhao Xing,[c] Xiangke Wang*[a,b] and An-Wu Xu*[c]

Three-dimensional hierarchical flower-like graphene oxide–hydroxyapatite (GO–HAp) nanocomposites were synthesized by a simple biomimetic method in a modified simulated body fluid (mSBF). The obtained GO–HAp nanocomposites were characterized by field-emission scanning electron microscopy (FE-SEM), transmission electron microscopy (TEM), X-ray diffraction (XRD), Fourier transformed infrared (FTIR) spectroscopy, X-ray photoelectron spectroscopy (XPS), Raman spectroscopy, and N_2 adsorption–desorption analysis. The formation mechanism was proposed and the prepared GO–HAp was applied as an adsorbent to remove strontium from large volumes of aqueous solutions. A maximum adsorption capacity of 702.18 mg g^{-1} was achieved on GO–HAp, almost two fold higher than that of bare HAp and nine fold higher than that of GO. The effects of pH, adsorbent content, contact time and Sr^{2+} initial concentrations on Sr^{2+} removal from solution by GO–HAp were systematically investigated, and the results indicated that the removal of Sr^{2+} by GO–HAp was weakly dependent on solution pH. The results herein reveal that the GO–HAp nanocomposites had exceptional potential as a suitable material for preconcentration and solidification of radiostrontium from large volumes of aqueous solutions in nuclear waste management and radiostrontium pollution cleanup.

1. Introduction

The removal of long-lived radionuclides from aqueous solutions has become a serious environmental problem all around the world. Leaking of radionuclides such as 90-Sr^{2+}, 137-Cs^+, UO_2^{2+}, and 129-I^- has aroused serious public concern because these fission products could make their way into the food chain when they are present in freshwater systems. Such radionuclides in contaminated water with high mobility will move into soils and finally end up in plant materials, ultimately becoming a part of animals and human beings. As a result of the earthquake and tsunami in the east coast of Japan on 11 March 2011, water as high as 15 m inundated the Fukushima Dai-ichi Nuclear Power Plant (NPP) that resulted in one of the

most important releases of artificial radioactivity to the environment.[1] Recently, high levels of radiostrontium (90-Sr^{2+}) have been found in groundwater at the devastated Fukushima nuclear power plant in Japan.[2] The radioisotope 90-Sr is one of the most critical radionuclides which can cause detrimental effects to animals and human beings because 90-Sr^{2+} can substitute for calcium in bones, leading to an increased risk of leukemia and other diseases.[3] Consequently, attenuation of strontium migration has been an actively pursued goal in water treatment. With the growing concern and better awareness of such environmental problems, a variety of technologies and materials have been investigated as means of attenuating strontium concentrations, such as adsorption, adsorption/ion-exchange, and biochemical reductive precipitation. The adsorption decontamination technique is regarded as the most promising process owing to it being inexpensive, effective, swift and environmentally friendly. Compared with traditional materials, nanomaterials possess faster rates and much higher efficiencies for contaminated water treatment due to their high surface areas, enhanced active sites, and abundant functional groups on the surfaces. Various advanced materials have been extensively adopted for the uptake of 90-Sr^{2+} ions from nuclear wastewater, such as graphene-based nanomaterials,[4,5] clay minerals,[6] zeolites,[7] titanate

[a]School for Radiological and Interdisciplinary Sciences, Soochow University, Suzhou 215123, P. R. China. E-mail: xkwang@ipp.ac.cn, xkwang@suda.edu.cn; Fax: +86-551-65591310; Tel: +86-551-65592788
[b]Institute of Plasma Physics, Chinese Academy of Sciences, Hefei, 230031, P. R. China
[c]Division of Nanomaterials and Chemistry, Hefei National Laboratory for Physical Sciences at Microscale Department, University of Science and Technology of China, Hefei, 230026, P. R. China. E-mail: anwuxu@ustc.edu.cn
†Electronic supplementary information (ESI) available. See DOI: 10.1039/c3dt53591f

nanotubes,[8] and layered sulfide frameworks.[9] Despite the fact that some outstanding results have been achieved, however, the inconvenience and complicated procedures in the preparation of nanomaterials have obviously restricted their practical applications. Thus, to design and to fabricate highly efficient nanoadsorbents in a low cost, simple and environmentally friendly way is a significant challenge for environmental pollution cleanup in real applications.

During the last decade, *in situ* growth of nanocomposites, an important bottom-up process, has been intensively developed as an effective and controllable strategy for the preparation of nanocomposites. Recently, Ariga *et al.*[10] reviewed the recent research of self-assembly, and concluded that self-assembly offered great possibilities for fabricating tailored multifunctional nanocomposites, attracting considerable attention for biomedicine,[11] energy science,[12] materials chemistry,[13] and environmental-related applications.[14,15] For example, in our previous study,[16] water-swellable LDHs–GO nanocomposites were *in situ* synthesized and used as adsorbents to effectively remove arsenic. Gong *et al.*[14] fabricated anisotropic layered double hydroxide nanocrystals@carbon nanospheres for efficient removal of heavy metal ions. Liu *et al.*[17] reported a novel process for the self-assembly of Fe_3O_4 nanoparticles onto titanate nanotubes, nanofibers, and nanosheets for water treatment. Herein we employed a biomimetic synthetic method to develop a simple and controllable self-assembly process to anchor hydroxyapatite (HAp) on the functional groups of graphene oxide (GO) nanosheets for the preparation of GO–HAp nanocomposites, in which strong interactions between the HAp tiny flakes and the GO nanosheets existed. The as-prepared HAp and GO–HAp nanocomposites were evaluated for the removal of Sr^{2+} from simulated wastewater. Graphene and graphene-based materials have been well-studied and demonstrated to be non-toxic and biodegradable, which make them a suitable adsorbent for environmental pollution management. The surface of GO is functionalized with many polar moieties such as carboxyl, epoxy and hydroxyl groups, which are essential for the capture of radionuclides. In general, hydroxyapatite ($Ca_{10}(PO_4)_6(OH)_2$, HAp) represents the main mineral component of biological hard tissues such as human bones and teeth. HAp has served as an inorganic exchanger in the remediation of soil and water from industrial and nuclear wastes due to its ability to retain a variety of ionic species, especially actinides and heavy metals.[18] To the best of our knowledge, no report is available on the elimination of Sr^{2+} by utilizing self-assembled GO–HAp nanostructures by a biomimetic synthetic route. Furthermore, the high potential of GO–HAp has been demonstrated by its excellent performance as a Sr^{2+} scavenger from contaminated water.

2. Experimental section

2.1 Chemicals

Graphite (99.999%, 325 mesh) was obtained from Alfa Aesar (Ward Hill, MA). 98% H_2SO_4, $KMnO_4$, 30% H_2O_2, $Sr(NO_3)_2$,

NaCl, $NaHCO_3$, Na_2SO_4, NaOH, $CaCl_2$, KCl, $K_2HPO_4·3H_2O$, $MgCl_2·6H_2O$ and HNO_3 were purchased from Sinopharm Chemical Reagent Company (China). The chemicals were obtained commercially and used directly without any further purification. Deionized water was used throughout the experiments. A stock solution of Sr^{2+} with a concentration of 1.0 g L^{-1} was prepared by dissolving strontium nitrate ($Sr(NO_3)_2$) into deionized water.

2.2 Synthesis of GO–HAp hybrid nanomaterials

Graphene oxide (GO) was synthesized *via* a modified Hummers method. Briefly, 0.3 g of GO powder was dispersed in 100 mL of water under ultrasonication for 1 hour, and the remaining unexfoliated GO was removed by centrifugation at 3000 rpm for 10 minutes. For the synthesis of GO–HAp, the above exfoliated GO (~0.282 g) was immersed in 1.5 × simulated body fluid (SBF) solution for 7 days of incubation. In order to ensure adequate ion concentrations for mineral growth, the mSBF solution was replaced daily. The 1.5 × simulated body fluid (1.5 × SBF) aqueous solution that had an ionic concentration 1.5 times higher than that of an SBF solution with an ion concentration close to human blood plasma, was prepared by dissolving 205.2 mM of NaCl, 6.3 mM of $NaHCO_3$, 0.75 mM of Na_2SO_4, 4.5 mM of KCl, 2.3 mM of $MgCl_2$, 3.8 mM of $CaCl_2$, and 1.5 mM of K_2HPO_4 in water, followed by buffering to pH 6.8 with Tris(hydroxymethyl) aminomethane (($CH_2OH)_3CNH_2$, Tris) at 37 °C in an incubator. After appropriate reaction time intervals, the precipitates were removed from the fluid, washed with deionized water three times and then dried at room temperature. For comparison, bare HAp was also synthesized by the aforementioned procedure without any GO addition.

2.3 The as-prepared GO–HAp for Sr^{2+} removal

The as-prepared HAp and GO–HAp stock suspension (3.0 g L^{-1}) were prepared by dissolution of HAp and GO–HAp into deionized water. The pH values of the suspensions were adjusted by adding small amounts of 0.01 or 0.1 M NaOH or HNO_3 solutions.

Batch adsorption experiments of Sr^{2+} onto HAp and GO–HAp were carried out in a polyethylene centrifuge tube at $T = 25 ± 2$ °C in the presence of 0.01 M $NaNO_3$. To evaluate the Sr^{2+} adsorption capacities, the stock solutions of HAp and GO–HAp, simulated wastewater with different Sr^{2+} concentrations ranging from 10 mg L^{-1} to 300 mg L^{-1}, and $NaNO_3$ were added to polyethylene tubes. For the kinetic studies, the dosages of the GO–HAp nanocomposites were maintained at 0.5 g L^{-1} at different Sr^{2+} concentrations (20, 60 and 100 mg L^{-1}). The solution mixtures were ultrasonicated at room temperature for 5 min and transferred to a rotary shaker for adsorption experiments. After appropriate time intervals, the solid phase was separated from the solution by centrifugation at 10 000 rpm for 10 min. The concentration of Sr^{2+} in the supernatant was determined by inductively coupled plasma (ICP) spectroscopy. The kinetic adsorption results indicated that the adsorption of Sr^{2+} on GO–HAp reached equilibration in several hours. To

investigate the effect of pH and GO–HAp content on Sr^{2+} adsorption, the Sr^{2+} solution was added to a 10 mL polyethylene centrifuge tube with different pH (2–11) and GO–HAp dosage (0.125–1.5 g L^{-1}). All experiments were carried out in triplicate.

2.4 Characterization

The morphologies and sizes of the as-synthesized HAp and GO–HAp were characterized by using field emission scanning electron microscopy (FE-SEM) (JEOL JSM-6330F) with a beam energy of 15.0 kV. Transmission electron microscopy (TEM) and high-resolution TEM (HR-TEM) (JEOL-2010) were applied to study the microstructures *via* dropping a small amount of sample onto a formbar-coated copper grid, followed by drying in air. The X-ray diffraction (XRD) measurements were performed on a Philips X'Pert Pro Super X-ray diffractometer with Cu Kα radiation (λ = 1.54178 Å). Fourier transformed infrared (FT-IR) spectroscopy was obtained by using a Nicolet Magana-IR 750 spectrometer over a range from 400 to 4000 cm^{-1}. Moreover, the surface states of the samples were characterized by X-ray photoelectron spectroscopy (XPS) using a VG Scientific ESCALAB Mark II spectrometer equipped with two ultrahigh vacuum (UHV) chambers. Raman spectra were obtained by using an InVia microscopic confocal Raman spectrometer (Renishaw, England) using a 514.5 nm laser beam. The N_2-BET (Barrett–Emmett–Teller) surface area was measured with a Micromeritics ASAP 2010 system at 77 K. The zeta potential values were measured using a ZETASIZER 3000 HSA system.

3. Results and discussion

3.1 Characterization of GO–HAp hybrid nanostructures

The morphological features of the as-prepared HAp and GO–HAp hybrid nanostructures were measured *via* FE-SEM and TEM. The pure HAp (Fig. 1a) appeared as typical stone-like aggregate features, containing a large number of tiny flakes, similar to the morphology observed in native bone tissue and in previous bioinspired mineral growth studies.[19] Fig. 1b and c display the SEM images at different magnifications of the as-prepared GO–HAp. Distinct from the conventional stone-like aggregates, three-dimensional (3D) flower-like hydroxyapatite crystals are wrapped with stretched GO nanosheets. 3D HAp crystals have extensively formed on the surface of the GO nanosheets and the GO sheets are incorporated in HAp crystals. This structure was also confirmed by the TEM image (Fig. 1d). The HR-TEM image shows the clear lattice fringes of GO and indistinct lattice fringes of HAp (Fig. S1†), indicating low crystallinity of the HAp deposited on the GO surfaces. The transparent and wrinkled GO nanosheets were attached on the HAp surfaces, which indicates the formation of the GO–HAp hybrid nanostructures. In addition, time-dependent SEM observations of GO incubated in modified simulated body fluid (mSBF) were carried out to gain an insight into the mechanism of nucleation and growth of hydroxyapatite on the 2D GO nanosheets (Fig. 2). At the early stages, we directly
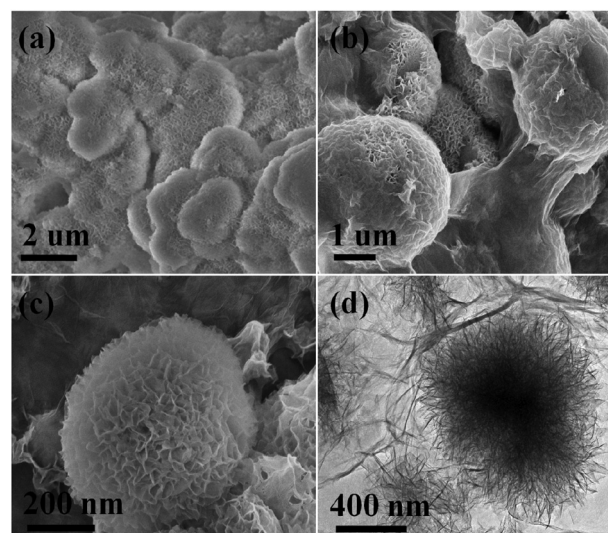

Fig. 1 Representative SEM image of (a) HAp, (b) low-magnification and (c) high-magnification images of GO−HAp, and (d) TEM image of GO−HAp.
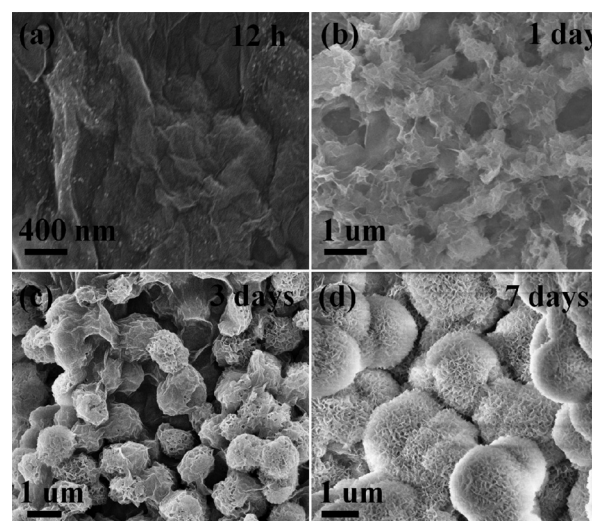

Fig. 2 Time-resolved process of mineral nucleation and growth on GO. SEM images of GO after (a) 12 h of immersion in 1.5 × SBF, (b) 1 day, (c) 3 days, and (d) 7 days.

observed the coagulation of GO in the mSBF solution on the macroscopic scale. During the 12 h of incubation in mSBF (Fig. 2a), the nucleation process began and small nanocrystals formed on the GO surface. Aggregation was a prerequisite for mineral nucleation and growth owing to the electrostatic interactions between the cations and the carboxyl-functionalized GO nanosheets. When the mineral crystallization time was extended to 1 day, 3D hierarchical structures assembled with nanoplate hydroxyapatite crystals appeared (Fig. 2b). On further prolonging the reaction time to 3 days, the collected sample displayed well-defined 3D flower-like nanostructures (Fig. 2c), ultimately growing into a continuous coating after 7 days (Fig. 2d). The morphological evolution with time of flower-
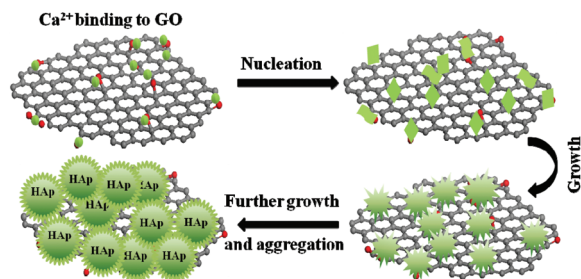
Published on 27 January 2014. Downloaded by Hefei Institutes of Physical Science, Chinese Academy of Sciences on 16/10/2015 02:35:25.

Dalton Transactions

Fig. 3 Schematic illustration of the morphological evolution process of the flower-like hierarchical GO–HAp nanocomposites.

like HAp, which were wrapped with GO nanosheets, clearly demonstrated that the GO–HAp nanostructures were formed *via* a stepwise growth mechanism.[20] Based on the above results of the SEM images, a plausible formation mechanism of the hierarchical flower-like GO–HAp is illustrated in Fig. 3. Graphene oxide with residing functional groups provided

binding sites to coordinate the major calcium cations, which suggested that mineral formation can be facilitated by aggregation. Therefore, these aggregates served as nucleation sites that allowed the subsequent adsorption of Ca^{2+} and the hydroxyapatite crystal growth on GO. After the prolonged incubation in mSBF solution, the precursors would further crystallize into lath-like nanostructures, generating a complete 3D hierarchical GO–HAp nanostructure.

The phase and composition of the GO–HAp sample after 7 days of incubation in 1.5 × SBF solution were characterized by XRD and FTIR spectroscopy. XRD can be used to identify the crystallographic structure and the results are shown in Fig. 4a. The XRD pattern of GO–HAp shows characteristic diffraction peaks (denoted by "H") at 2θ = 26.02°, 28.96°, 32.2°, and 39.8°, consistent with the XRD pattern of pure HAp. The broadness of the diffraction peaks may be due to the low crystallinity or the ultrafine nano-crystallinity of HAp deposited on the GO surfaces, which is consistent with HR-TEM analysis.[21] In addition, a broad and relatively weak diffraction peak at 2θ =
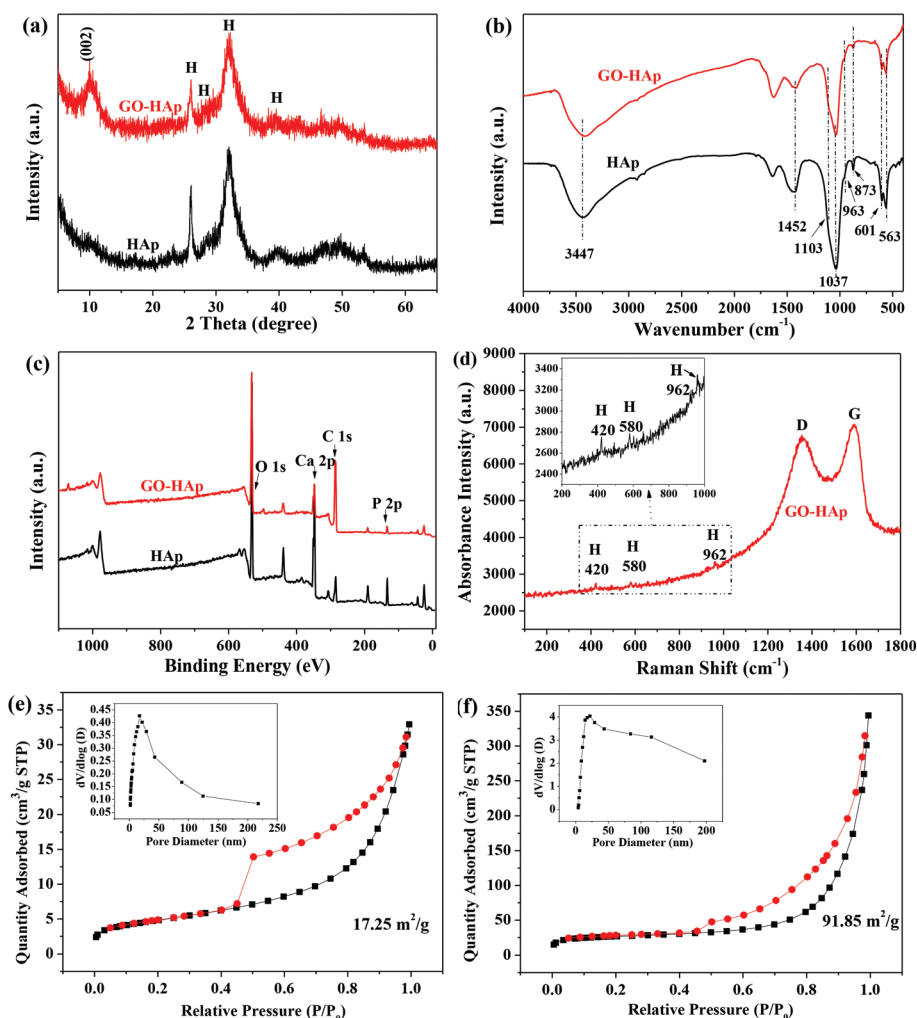

Fig. 4 (a) XRD patterns; (b) FTIR spectra; (c) XPS spectra and (d) Raman spectrum of the as-prepared HAp and GO–HAp samples after 7 days of incubation in 1.5 × SBF solution. N$_2$ adsorption–desorption isotherms of the as-prepared (e) HAp and (f) GO–HAp samples. The insets show the corresponding pore size distribution curves.

This journal is © The Royal Society of Chemistry 2014

Dalton Trans., 2014, **43**, 7464–7472 | **7467**

10.03° was attributed to the (002) plane, which corresponded to the typical diffraction peak of GO nanosheets.[22] No peaks from impurities were detected by XRD analysis. The FTIR spectra of the HAp and GO–HAp samples are displayed in Fig. 4b. The absorption peaks appearing at 563, 601, 963, 1037, and 1103 cm⁻¹ were ascribed to phosphate, and the peaks at 873 cm⁻¹ and 1452 cm⁻¹ were attributed to the carbonate group.[23] Therefore, the HAp nanocrystal, which formed on the surfaces of GO, was carbonate-containing hydroxyapatite. Moreover, the relatively weak intensity peak at 963 cm⁻¹, which can be assigned to protonated phosphate ions (HPO_4^{2-}), was due to the incubation in a modified simulated body fluid buffered to pH 6.8 with Tris.[23] The strong peak at 3447 cm⁻¹ was attributed to the stretching modes of the OH groups associated with the structure of HAp ($Ca_{10}(PO_4)_6(OH)_2$) and GO. XPS analysis further confirmed the presence of phosphorus and calcium in the GO–HAp sample (Fig. 4c). The Ca/P molar ratio of GO–HAp (1.84) after mineral coating was higher than that of HAp (1.58), which was not in agreement with the structural formula of hydroxyapatite. This difference was mainly attributed to the residing functional groups of GO, such as carboxylic acid, hydroxyl, epoxy, and other carbonyl groups,[24] which can favorably interact with Ca^{2+} in mSBF solution, leading to the higher Ca/P molar ratio in GO–HAp sample. In addition, the intensity of C 1s in GO–HAp was much higher than that of C 1s in pure HAp (Fig. 4c), indicating that the graphene was incorporated with hydroxyapatite. Further structural characterization by Raman spectroscopy demonstrated the coexistence of HAp and GO in the sample (Fig. 4d). The Raman spectrum of GO–HAp showed the characteristic peaks of HAp (denoted by "H") at 420, 580, and 962 cm⁻¹, which are associated with the P–O vibration, O–P–O vibration, and P–O stretching, respectively.[25–27] As is clear from the Raman spectrum of the GO–HAp sample, the exclusive characteristic D and G bands at 1354 and 1592 cm⁻¹ can be found and match with the first-order spectra of graphene nanosheets. The intensity ratio of the D peak to G peak usually reflects the order of defects in GO and the calculated I_D/I_G value is about 0.96, implying that the chemical oxidation has introduced considerable structural disorders in the graphene lattice.

The N_2 adsorption–desorption isotherms of HAp and GO–HAp were measured utilizing the BET method for specific surface area calculation. As shown in Fig. 4e and f, type IV isotherms with obvious type H3 hysteresis loops were observed for the as-prepared samples, indicating the presence of mesoporous architecture and tiny nanoflake aggregates. This result was in good agreement with the results of SEM and TEM images. The corresponding pore size distribution curves are shown in the inset of Fig. 4e and f, it can be seen that the centered pore size distribution of GO–HAp derived from the desorption branch, by the BJH model, increased slightly from the pure HAp (17.4 nm) to the as-prepared GO–HAp (22.1 nm). The specific surface areas of GO–HAp and pure HAp were about 91.85 and 17.25 m² g⁻¹, respectively, suggesting that the specific surface area of GO–HAp was largely increased through the graphene-incorporated HAp as compared with that of bare HAp.

3.2 Kinetic study of Sr^{2+} adsorption on GO–HAp

To evaluate the adsorption ability of GO–HAp, batch adsorption experiments were performed. Sr^{2+} adsorption by GO–HAp at different Sr^{2+} concentrations is shown in Fig. 5a. It was evident that the Sr^{2+} adsorption rate was considerably quick within the initial contact time of 1 h at initial concentrations of 20, 60 and 100 mg L⁻¹. At the initial concentration of 20 mg L⁻¹, the adsorption of Sr^{2+} on GO–HAp quickly reached equilibrium in 2 h and more than 80% of the Sr^{2+} ions was removed from aqueous solution. In comparison, for the concentrations of 60 and 100 mg L⁻¹, the adsorption of Sr^{2+} on GO–HAp took place in two distinct stages: a relatively fast removal stage followed by a slow increase stage until the state of equilibrium was reached. The fast removal stage indicated that strong chemisorption or surface complexation dominated the adsorption of Sr^{2+} on GO–HAp. Meanwhile, the unique HAp selectivity towards divalent metal cations was a result of the ion-exchange process with Ca^{2+} ions.[28] Thus, as the contact time increased, the Ca^{2+} ions in the interlayers of the HAp were gradually replaced by Sr^{2+} ions, which were immobilized in the interlayers. When the surface adsorption sites became exhausted, the rate of adsorption was controlled by the rate of intraparticle diffusion from the exterior to the interior sites of the adsorbent, which resulted in the relative slower removal stage.[17,28] Finally, the adsorption equilibrium was reached slowly with increasing contact time. Meanwhile, the influence of incubation time of GO–HAp on the removal of Sr^{2+} was also investigated. As shown in Fig. S2,† the percentage of Sr^{2+} removal on GO–HAp with 12 h of incubation was about 60%, which was very close to the removal percentage of GO. Then, the adsorption percentage of Sr^{2+} increased gradually with increasing mineral time. Finally, the adsorption percentage maintained a relatively high value (~95.0%) using the GO–HAp with further prolonging incubation time to 5 and 7 days.

A pseudo-second-order rate model was applied to simulate the experimental data in order to determine the adsorption rate constant at room temperature. The pseudo-second-order rate expression was defined by eqn (1):

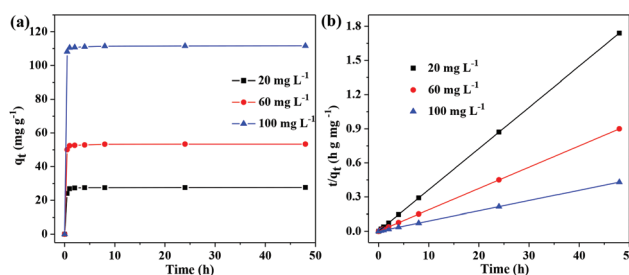$$\frac{t}{q_t} = \frac{1}{k_2 q_e^2} + \frac{t}{q_e} \tag{1}$$

Fig. 5 (a) The influence of contact time on the removal of Sr^{2+} and (b) linear fit of experimental data obtained using a pseudo-second-order kinetic model at different initial Sr^{2+} concentrations, pH = 7.0 ± 0.1, m/V = 0.5 g L⁻¹, and I = 0.01 M NaNO₃.

where q_t (mg g^{-1}) and q_e (mg g^{-1}) were the amounts of Sr^{2+} adsorbed at contact time t (h) and equilibrium, respectively; k_2 (g (mg h)$^{-1}$) was the equilibrium rate constant of pseudo-second-order. The kinetic adsorption is shown in Fig. 5b. As can be seen from the removal time profile, the total amount of Sr^{2+} adsorbed increased with increasing Sr^{2+} concentrations. The kinetics parameters obtained in fitting the experimental data are summarized in Table 1. The high correlation coefficient and the agreement of calculated and experimental q_e values at different Sr^{2+} concentrations both suggested that the removal kinetics followed the pseudo-second-order model. It was emphasized that at a low concentration of 20 mg L^{-1}, the adsorption of Sr^{2+} on GO–HAp reached equilibrium swiftly with a rate constant k_2 of 1.15 g (mg h)$^{-1}$, which was higher than that of Sr^{2+} at high Sr^{2+} concentrations.

3.3 Effect of solution pH on Sr^{2+} adsorption

The effect of pH on the removal of Sr^{2+} by GO–HAp was also investigated in the pH range of 2–11. Fig. 6a showed that the percentage of Sr^{2+} removal remained very high (90%) in a wide pH range (5–11), and more than 76% Sr^{2+} was adsorbed on GO–HAp even at low pH (pH 2–4). Our GO–HAp sample showed better performance under acidic conditions as compared with the traditional ion exchangers.[29] From the results of the zeta-potential values (Fig. 6b), the electrostatic point of GO–HAp was negative in the pH range of 2–11. This was mainly due to the unique physicochemical properties of the HAp interface. As mentioned in a previous report, the as-prepared HAp exhibited excellent buffering properties.[30] The following acid–base reactions could be responsible for the surface protonation and deprotonation reactions of GO–HAp in aqueous solutions:

$$\equiv PO^- + H^+ \Leftrightarrow \equiv POH^0 \tag{2}$$

$$\equiv CaOH_2{}^+ \Leftrightarrow \equiv CaOH^0 + H^+ \tag{3}$$

Generally, the positively charged $\equiv CaOH_2{}^+$ and neutral $\equiv POH^0$ are predominant species on the surface of GO–HAp at low pH because of the protonation reaction. However, with an increase of the initial pH, the surface charges of GO–HAp become negative because of OH$^-$ consumption via the deprotonation reaction, indicating that $\equiv CaOH^0$ and $\equiv POH^-$ are the main sites on the surface of GO–HAp in alkaline solutions.[28] However, the electrostatic point of GO–HAp in our experiments was negative on the surface of GO–HAp throughout the pH region (2–11). The GO incorporated HAp should be taken into account for the decrease of pH$_{pzc}$, which shifted to lower pH. The zeta-potential value of GO–HAp could explain the high capture of Sr^{2+} at low pH values. This result was consistent with a recent study about the capture of uranium on layered metal sulfides from seawater.[9] The results highlighted that GO–HAp nanocomposites could preconcentrate the Sr^{2+} ions from aqueous solutions without adjusting the initial pH values.

### 3.4. Effect of coexisting cations and GO–HAp content on Sr^{2+} adsorption

The effect of coexisting cations on Sr^{2+} adsorption is shown in Fig. S3.† All batch adsorptions of Sr^{2+} on GO–HAp were carried out in the presence of various inorganic cations (I = 0.01 M). It can be seen that the removal percent of Sr^{2+} was slightly influenced by the cations of Cd^{2+} and Pb^{2+}, whereas in the presence of Mg^{2+}, Al^{3+} and Na$^+$, one can see that they had no obvious effect on Sr^{2+} adsorption onto GO–HAp. In previous studies, two ionic species may only exchange if their ionic radius cannot differ in size by more than 15%.[31] The little inhibiting effect of Sr^{2+} could be due to the competition in adsorption of Cd^{2+} and Pb^{2+} with Sr^{2+}. Adsorbent dosage is an important parameter which determines the capacity of an adsorbent for a given initial concentration of the adsorbate. The amounts of uptake as a function of the adsorbent content are shown in Fig. 7a. A significant relationship was observed that the adsorption percentage of Sr^{2+} increased swiftly with increasing GO–HAp content. The tendency may be explained that upon increasing adsorbent amount, the number of surface active sites on the GO–HAp increased, which are favorable for the binding of Sr^{2+}. Fig. 7a also shows that the distribution coefficient (K_d) of Sr^{2+} on GO–HAp decreased gradually with the increase of solid content. The decrease of K_d value was ascribed to the fact that the surface active sites were entirely exposed for sorption and the Sr^{2+} ions can easily access the adsorption sites with high q_e at a low adsorbent amount, whereas at higher adsorbent amounts, the amount adsorbed per unit mass of adsorbent decreased considerably owing to particle aggregation, which led to a decrease in the total

Table 1 Experimental and calculated q_e values, pseudo-second-order rate constants, k_2, and correlation coefficient values, R^2

Initial concentration of Sr^{2+} (mg L^{-1})	Experimental values q_e (mg g^{-1})	Calculated q_e (mg g^{-1})	k_2 (g (mg h)$^{-1}$)	R^2
20	27.59	27.60	1.1514	0.9993
60	53.39	53.42	0.8316	0.9996
100	111.61	111.61	0.6456	0.9999
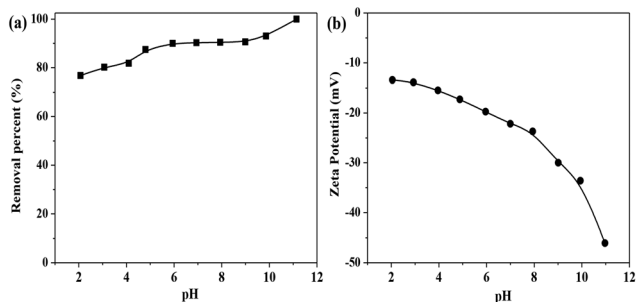
Fig. 6 (a) Effect of solution pH on the adsorption of Sr^{2+} on GO–HAp. (b) Zeta-potential of GO–HAp as a function of pH. All batch adsorptions were conducted in C[Sr^{2+}]$_{initial}$ = 20 mg L^{-1}, m/V = 0.5 g L^{-1}, and I = 0.01 M NaNO$_3$ in a polyethylene test tube.
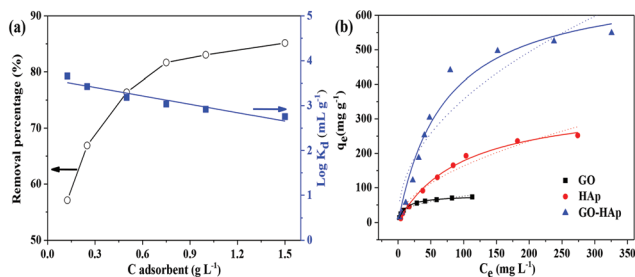
Fig. 7 (a) Removal of Sr^{2+} from solution onto GO–HAp as a function of GO–HAp content, pH = 7.0 ± 0.1, $C[Sr^{2+}]_{initial}$ = 20 mg L^{-1}, and I = 0.01 M $NaNO_3$. (b) Adsorption isotherms of Sr^{2+} on GO, HAp and GO–HAp samples. Symbols denote experimental data, the solid lines represent the Langmuir model simulation, the dashed lines represent the Freundlich model. All adsorption isotherms were conducted at pH = 7.0 ± 0.1, m/V = 0.5 g L^{-1}, and I = 0.01 M $NaNO_3$ polyethylene test tube.

surface area and an increase in diffusional path length,[32] thus resulting in the decrease of distribution coefficient.

3.5 Adsorption isotherms

To evaluate the Sr^{2+} removal performance of the adsorbents, the adsorption capacity of GO–HAp for Sr^{2+} was compared with those of bare GO and HAp. Both the Langmuir and Freundlich isotherms were used to describe the adsorption behavior of Sr^{2+}. In general, the Langmuir model is applicable to a homogeneous adsorption surface with all the adsorption sites having the same sorption energy independent of surface coverage, whereas the Freundlich isotherm model assumes a heterogeneous adsorption surface.[15] The two adsorption models can be expressed by the following equations:

$$\text{Langmuir model}: q_e = \frac{bq_{max}C_e}{1 + bC_e} \quad (4)$$

$$\text{Freundlich model}: q_e = kC_e^{1/n} \quad (5)$$

where C_e (mg L^{-1}) is the Sr^{2+} equilibrium solute concentration and q_e (mg g^{-1}) is the amount of Sr^{2+} adsorbed per weight of adsorbent after adsorption equilibrium. q_{max} (mg g^{-1}) is the maximum adsorption capacity at complete monolayer coverage and b (L mg^{-1}) is a Langmuir constant. The k value is correlated to the relative adsorption capacity of the adsorbent (mg g^{-1}), and n is related to the energetic heterogeneity. Table 2 summarizes the corresponding maximum adsorption capacity, q_{max}, relating to the constants and correlation coefficients involved in the two isotherm models, clearly indicating that both the Langmuir and Freundlich models fitted the Sr^{2+} adsorption isotherm well. The Langmuir model fitted the sorption isotherms better than the Freundlich model, which may be attributed to the homogeneous distribution of active sites on the GO–HAp surface. From the Langmuir adsorption model, the highest adsorption capacity of the as-prepared GO–HAp was calculated to be 702.18 mg g^{-1}, almost two fold higher than that of bare HAp. The highest adsorption capacity of Sr^{2+} on GO (78.19 mg g^{-1}) was higher than that of GO reported previously (23.83 mg g^{-1}),[4] which was mainly

Table 2 Summary of the Langmuir and Freundlich isotherm model parameters for Sr^{2+} uptake capacity on GO, HAp and GO–HAp

Samples	Langmuir			Freundlich		
	q_{max} (mg g^{-1})	b (L mg^{-1})	R^2	k	n	R^2
GO	78.19	0.0931	0.993	17.20	3.10	0.952
HAp	354.60	0.0101	0.994	14.44	1.90	0.952
GO–HAp	702.18	0.0139	0.968	41.13	2.13	0.889

attributed to the pre-oxidization process and the residing functional groups of GO. According to the BET surface area measured above, the as-prepared GO–HAp possessed a considerably higher specific surface area (91.85 m^2 g^{-1}) compared with bare HAp (17.25 m^2 g^{-1}). Therefore, the high surface area of the GO–HAp nanocomposite was one factor to afford the high-performance in water treatment. Table 3 shows the comparison of Sr^{2+} adsorption capacities for various adsorbents, such as natural clinoptilolite (9.80 mg g^{-1}),[33] graphene oxide (23.83 mg g^{-1}),[4] titanate nanofibers (55.20 mg g^{-1}),[34] carboxymethylated cellulose (108.7 mg g^{-1}),[35] pecan shells (180 mg g^{-1}),[36] and biogenic hydroxyapatite (34.17 mg g^{-1}).[37] One can see that the prepared GO–HAp nanocomposite exhibited a highly efficient sorption capacity toward Sr^{2+} ions and has potential applications for practical water treatment in real applications.

3.6 Adsorption mechanism

To further investigate the interaction mechanism between Sr^{2+} and the GO–HAp composite, the high resolution XPS scans for Ca 2p, P 2p, O 1s and Sr 3d before and after Sr^{2+} adsorption were measured. As shown in Fig. 8a, the Sr^{2+} peak was observed in Sr^{2+}-adsorbed GO–HAp and the doublet peak characteristic of Sr 3d appeared at 133.98 eV and 135.68 eV, which can be assigned to Sr $3d_{5/2}$ and Sr $3d_{3/2}$, respectively. Fig. 8b shows the relative intensity of Ca 2p peaks at 347.4 eV and 350.9 eV after Sr^{2+} adsorption were much lower than those of the Ca 2p peaks of GO–HAp before Sr^{2+} adsorption, suggesting the partial replacement of Ca^{2+} by Sr^{2+}. Furthermore, there were some calcium cations which were not completely exchanged by Sr^{2+} bound on graphene oxide by the residing functional groups. Meanwhile, the high resolution P 2p and O 1s spectra were also investigated (Fig. 8c and d). An apparent

Table 3 Comparison of the maximum adsorption capacities of Sr^{2+} on GO–HAp with other different adsorbents

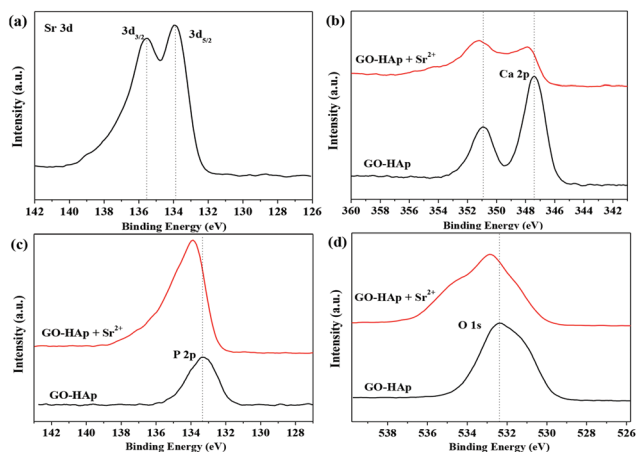| Adsorbents	pH	Adsorption capacity (mg g^{-1})	References
Natural clinoptilolite	7.0	9.80	34
Graphene oxide	6.5	23.83	4
Titanate nanofibers	7.0	55.20	35
Carboxymethylated cellulose	4.0	108.7	36
Pecan shells	8.5	180	37
Biogenic hydroxyapatite	7.0	34.17	38
Hap	7.0	354.60	This study
GO–HAp	7.0	702.18	This study

Fig. 8 XPS high resolution spectra of (a) Sr 3d, of the Sr^{2+}-adsorbed sample; (b) Ca 2p, (c) P 2p, and (d) O 1s before and after Sr^{2+} adsorption.

shift could be observed after Sr^{2+} adsorption, which indicated the alteration of the local bonding environments.

According to the above discussion, we suppose that there are two possible mechanisms of Sr^{2+} adsorption: ion-exchange and the formation of complex compounds with HAp active surface sites.[38] The solution ionic radius of Sr^{2+} (0.125 nm) is similar in size to the Ca^{2+} ion (0.103 nm).[39] The ion-exchange of these two metals is thought to be the mechanism of removal in aqueous water. What's more, H^+ ions could be liberated from the solid surface into the aqueous phase as a result of the exchange with ions, contributing to the formation of surface complexes:

$$HAp\text{–}Ca^{2+} + Sr_{aq}^{2+} \Leftrightarrow HAp\text{–}O\text{–}Sr^{2+} + Ca_{aq}^{2+} \quad (6)$$

$$HAp\text{–}OH + Sr_{aq}^{2+} \Leftrightarrow HAp\text{–}O\text{–}Sr^{2+} + H_{aq}^{+} \quad (7)$$

$$2HAp\text{–}OH + Sr^{2+} \Leftrightarrow (HAp\text{–}O)_2Sr + 2H^+ \quad (8)$$

4. Conclusions

In conclusion, we have developed graphene oxide–hydroxyapatite nanocomposites for highly efficient removal of Sr^{2+} by a simple biomimetic synthetic method in mSBF, and a formation mechanism for the hierarchical flower-like GO–HAp nanostructures was proposed. Batch adsorption experiments showed that GO–HAp can completely remove Sr^{2+} from simulated wastewater within 2 h for various initial Sr^{2+} concentrations. The results demonstrated that Sr^{2+} ion adsorption on GO–HAp was weakly dependent on solution pH, which can be explained by the zeta-potential values of the surface of GO–HAp. With relatively high specific surface areas, the 3D hierarchical flower-like GO–HAp nanostructures showed a remarkably high exchange capacity and affinity for Sr^{2+} ions. A maximum adsorption capacity of 702.18 mg g^{-1} was achieved over GO–HAp, which was the highest value reported for todays' materials. The biomineral based GO–HAp nanocomposites

could be a suitable material for the preconcentration and solidification of radiostrontium from large volumes of aqueous solutions in radionuclide environmental pollution purification in the near future.

Notes and references

1 K. Buesseler, M. Aoyama and M. Fukasawa, *Environ. Sci. Technol.*, 2011, **45**, 9931–9935.
2 A. Slodkowski, News Press Releases http://uk.reuters.com// article/2013/10/21/ (accessed Oct 21, 2013).
3 S. Nielsen, *Bone*, 2004, **35**, 583–588.
4 A. Romanchuk, A. Slesarev, S. Kalmykov, D. Kosynkin and J. Tour, *Phys. Chem. Chem. Phys.*, 2013, **15**, 2321–2327.
5 G. Zhao, L. Jiang, Y. He, J. Li, H. Dong, X. Wang and W. Hu, *Adv. Mater.*, 2011, **23**, 3959–3963.
6 J. Yoo, T. Shinagawa, J. Wood, W. Linak, D. Santoianni, C. King, Y. Seo and J. Wendt, *Environ. Sci. Technol.*, 2005, **39**, 5087–5094.
7 D. Marinin and G. Brown, *Waste Manage.*, 2000, **20**, 545–553.
8 D. Yang, S. Sarina, H. Zhu, H. Liu, Z. Zheng, M. Xie, S. Smith and S. Komarneni, *Angew. Chem., Int. Ed.*, 2011, **50**, 10594–10598.
9 M. Manos and M. Kanatzidis, *J. Am. Chem. Soc.*, 2012, **134**, 16441–16446.
10 K. Ariga, J. Hill, M. Lee, A. Vinu, R. Charvet and S. Acharya, *Sci. Technol. Adv. Mater.*, 2008, **9**, 014109.
11 Y. Jin, C. Jia, S. Huang, M. O'Donnell and X. Gao, *Nat. Commun.*, 2010, **1**, 41.
12 S. Yang, X. Wu, C. Chen, H. Dong, W. Hu and X. Wang, *Chem. Commun.*, 2012, **48**, 2773–2775.
13 X. Sun and Y. Li, *Angew. Chem., Int. Ed.*, 2004, **43**, 597–601.
14 J. Gong, T. Liu, X. Wang, X. Hu and L. Zhang, *Environ. Sci. Technol.*, 2011, **45**, 6181–6187.
15 V. Chandra, J. Park, Y. Chun, J. Lee, I. Hwang and K. Kim, *ACS Nano*, 2010, **4**, 3979–3986.
16 T. Wen, X. Wu, X. Tan, X. Wang and A. Xu, *ACS Appl. Mater. Interfaces*, 2013, **5**, 3304–3311.
17 F. Liu, Y. Jin, H. Liao, L. Cai, M. Tong and Y. Hou, *J. Mater. Chem. A*, 2013, **1**, 805–813.
18 F. Rivera and M. Fedoroff, in *Encyclopedia of Surface and Colloid Science*. Marcel Dekker. Inc., 2002, pp. 1–26.
19 L. Jongpaiboonkit, T. Franklin-Ford and W. Murphy, *ACS Appl. Mater. Interfaces*, 2009, **1**, 1504–1511.

20 X. Yu, T. Luo, Y. Jia, R. Xu, C. Gao, Y. Zhang, J. Liu and X. Huang, *Nanoscale*, 2012, **4**, 3466–3474.

21 S. Rhee and J. Tanaka, *J. Am. Ceram. Soc.*, 1998, **81**, 3029–3031.

22 G. Zhao, J. Li, X. Ren, C. Chen and X. Wang, *Environ. Sci. Technol.*, 2011, **45**, 10454–10462.

23 S. Choi and W. Murphy, *J. Mater. Chem.*, 2012, **22**, 25288–25295.

24 W. Gao, L. Alemany, L. Ci and P. Ajayan, *Nat. Chem.*, 2009, **1**, 403–408.

25 A. Antonakos, E. Liarokapis and T. Leventouri, *Biomaterials*, 2007, **28**, 3043–3054.

26 S. Kim, S. Ku, S. Lim, J. Kim and C. Park, *Adv. Mater.*, 2011, **23**, 2009–2014.

27 I. Smiciklas, S. Dimovic, I. Plecas and M. Mitric, *Water Res.*, 2006, **40**, 2267–2274.

28 F. Acar and E. Malkoc, *Bioresour. Technol.*, 2004, **94**, 13–15.

29 L. Al-Attar and A. Dyer, *J. Mater. Chem.*, 2002, **12**, 1381–1386.

30 I. Smiciklas, S. Milonjic, P. Pfendt and S. Raicevic, *Sep. Purif. Technol.*, 2000, **18**, 185–194.

31 J. Reichert and J. Binner, *J. Mater. Sci.*, 1996, **31**, 1231–1241.

32 K. Bhattacharyya and S. Gupta, *Appl. Clay Sci.*, 2008, **41**, 1–9.

33 I. Smičiklas, S. Dimović and I. Plećaš, *Appl. Clay Sci.*, 2007, **35**, 139–144.

34 D. Yang, Z. Zheng, H. Liu, H. Zhu, X. Ke, Y. Xu, D. Wu and Y. Sun, *J. Phys. Chem. C*, 2008, **112**, 16275–16280.

35 M. Wang, L. Xu, J. Peng, M. Zhai, J. Li and G. Wei, *J. Hazard. Mater.*, 2009, **171**, 820–826.

36 R. Shawabkeh, D. Rockstraw and R. Bhada, *Carbon*, 2002, **40**, 781–786.

37 S. Handley, J. Renshaw, S. Moriyama, B. Stolpe, C. Mennan, S. Bagheriasl, P. Yong, A. Stamboulis, B. Paterson, K. Sasaki, R. Pattrick, J. Lead and L. Macaskie, *Environ. Sci. Technol.*, 2011, **45**, 6985–6990.

38 I. Smičiklas, S. Dimović, M. Šljivić and I. Plećaš, *J. Environ. Sci. Health, Part A: Toxic/Hazard. Subst. Environ. Eng.*, 2008, **48**, 210–217.

39 Y. Marcus, *Chem. Rev.*, 1988, **88**, 1475–1498.